# Oxygenated Surface of Carbon Nanotube Sponges: Electroactivity and Magnetic Studies

Alejandro J. Cortés-López, Emilio Muñoz-Sandoval, and Florentino López-Urías*

División de Materiales Avanzados, IPICYT, Camino a la Presa San José 2055, Lomas 4a Sección, San Luis Potosí, San Luis Potosí 78216, México

Ⓢ Supporting Information

ABSTRACT: We report the synthesis of nitrogen-doped carbon nanotube sponges (N-CNSs) by pyrolysis of solutions of benzylamine, ferrocene, thiophene, and isopropanol-based mixture at 1020 °C for 4 h using an aerosol-assisted chemical vapor deposition system. The precursors were transported through a quartz tube using a dynamic flow of H_2/Ar. We characterized the N-CNSs by scanning electron microscopy, transmission electron microscopy, X-ray diffraction, X-ray photoelectron spectroscopy, Fourier transform infrared spectroscopy, Raman spectroscopy, and thermogravimetric analysis. We found that isopropanol, isopropanol−ethanol, and isopropanol−acetone as precursors promote the formation of complex-entangled carbon fibers making knots and junctions. The N-CNSs displayed an outstanding oxygen concentration reaching a value of 9.2% for those synthesized with only isopropanol. We identified oxygen and nitrogen functional groups; in particular, the carbon fibers produced using only isopropanol exhibited a high concentration of ether groups (C−O bonds). This fact suggests the presence of phenols, carboxyl, methoxy, ethoxy, epoxy, and more complex functional groups. Usually, the functionalization of graphitic materials is carried out through aggressive acid treatments; here, we offer an alternative route to produce a superoxygenated surface. The understanding of the chemical surface of these novel materials represents a huge challenge and offers an opportunity to study complex oxygen functional groups different from the conventional quinone, carboxyl, phenols, carbonyl, methoxy, ethoxy, among others. The cyclic voltammetry measurements confirmed the importance of oxygen in N-CNSs, showing that with high oxygen concentration, the highest anodic and cathodic currents are displayed. N-CNSs displayed ferromagnetic behavior with an outstanding saturation magnetization. We envisage that our sponges are promising for anodes in lithium-ion batteries and magnetic sensor devices.
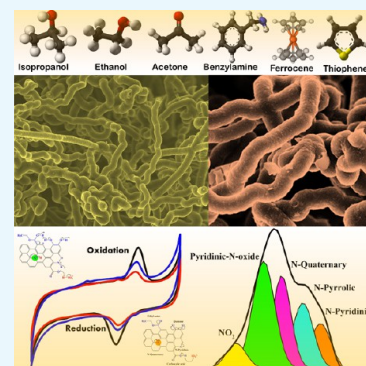
1. INTRODUCTION

Carbon nanotube sponges (CNSs) are three-dimensional networks of interconnected carbon nanotubes with outstanding physical and chemical properties such as super-hydrophobicity,[1] surface chemical functionalization,[2] porosity,[3] elasticity,[4−6] electrical conductivity,[7] low thermal conductivity,[8] and high energy dissipation.[9] CNSs have also been used as filter nanoparticles,[10] absorb oils,[1,11−14] transport nanoparticles,[15] supercapacitors,[16−18] fuel cells,[19] electrodes,[20,21] deionize water,[22] and as scaffolds for cell seeding in biological applications.[23]

The chemical vapor deposition (CVD) method has been the most common method to produce CNSs.[24,25] Gui et al.[1] reported using the CVD method, the production of CNSs. They used a solution containing 1,2-dichlorobenzene and ferrocene as precursors. Their CNSs showed flexibility and capacity for oil absorption reaching up to ~170 times its weight. They also reported in other investigation using a similar experimental approach the production of sponges formed by carbon nanotubes with Fe inside.[26] Shan et al.[7] synthesized three-dimensional CNSs using ferrocene, thiophene, and pyridine by the CVD method. Their carbon sponge exhibited welded junctions and elbows formed by the presence

of nitrogen that boosted a three-dimensional growth. They demonstrated that sulfur concentration plays a role in tuning the diameters of carbon nanotubes. Camilli et al.[14] fabricated three-dimensional CNSs using ferrocene, thiophene, and ethanol by the CVD method; their sponges were superlight and superhydrophobic with outstanding electrical conductivity and reversible compressibility.

Zhao et al.[27] synthesized CNSs by the CVD method using ferrocene, toluene, triethylborane, thiophene, and pyridine as precursors. They produced nitrogen- and boron-doped carbon sponges and found that the concentration of thiophene controlled the average diameter of carbon nanotubes. Hashim et al.[28] produced boron-doped CNSs using toluene, ferrocene, and triethylborane by the CVD method. Carbon sponges can also be fabricated using gas precursors. For instance, Erbay et al.[19] synthesized CNSs using ethylene gas and ferrocene. They used the CNSs as an anode in microbial fuel cells, generating a high power density of ~2100 Wm^{-3} per anode volume.

It has already been proved that alcohols are excellent precursors for the synthesis of single-walled and multiwalled carbon nanotubes by the CVD method: methanol,[29,30] ethanol,[31−36] methanol/ethanol mixtures,[34] isopropanol,[35] and hexanol.[35] Recently, alcohols have also been used to produce CNSs, for example, ethanol[2,36] and ethanol−acetone solutions.[37] The chemical species arising by the thermal decomposition of alcohols provide possible routes for the growth of N-CNSs in an aerosol-assisted chemical vapor deposition (AACVD) experiment.[37] In this work, we focus our investigation on the use of isopropanol as a carbon precursor. The chemical species arising during its particular thermal decomposition (propylene and water)[38] offers insights into the formation of novel carbon nanostructures with interesting physical−chemical properties. Furthermore, the thermal decomposition of propylene produces ethylene and methylene.[39] Ethylene is an excellent precursor for the synthesis of carbon nanotubes in conjunction with water,[40−42] and methylene is a very reactive chemical species, which could favor the size increment of carbon chains or rings.[43]

In this article, we report the use of isopropanol-based mixture and benzylamine as precursors to produce nitrogen-doped CNSs (N-CNSs) by the AACVD method. We demonstrated that isopropanol yields entangled carbon nanotubes with nitrogen and oxygen functional groups on their surface. We have also investigated the role of other alcohols (solutions containing isopropanol−ethanol and isopropanol−acetone) on the morphology, chemical surface, and absorption properties of carbon sponges. We discuss the magnetic properties and electrochemical activity of carbon sponges. Our results demonstrated that N-CNSs synthesized with isopropanol have high oxygen concentration at their surface with outstanding anodic and cathodic currents with potential applications in energy storage devices.

2. RESULTS AND DISCUSSION

Figure 1 displays scanning electron microscopy (SEM) images for samples S1, S2, and S3. The sponges contain complex entangled carbon fibers making knots and junctions (see yellow arrows). The carbon fibers showed straight and curly morphologies indicated by white arrows. Predominantly, the straight fibers were thinner than curly fibers. Sample S3 displayed the thinnest straight fibers (Figure 1e) with a diameter of up to 80 nm. Backscattered electrons and energy-dispersive spectroscopy (EDS) images of S1, S2, and S3 are displayed in Figure SI-1, revealing that all samples contain mainly C, O, and Fe. Figure SI-2 shows the diameter distribution plots for S1, S2, and S3. Sample S2 displayed the largest average diameter (514.2 nm), followed by S1 (443.8 nm), and finally S3 with two modal curves with a smaller mean diameter (160.96 and 284.06 nm). Concerning yield production, we collected 8.80, 5.88, and 15.71 g for S1, S2, and S3, respectively. Therefore, the solution S-IA (isopropanol−acetone 1:1) is an efficient precursor to increase the yield production. Recently, we reported that the ethanol−acetone 1:1 solution as a precursor in an AACVD experiment also increases the yield production.[37] The chemical species released during the thermal decomposition of isopropanol, ethanol, and acetone could give insights into the growth mechanism of carbon fibers that constitute the N-CNS. The thermal decomposition of isopropanol releases propylene and water,[38] ethanol releases ethylene and water,[44] and acetone releases methyls and carbon monoxide.[45] The thermal
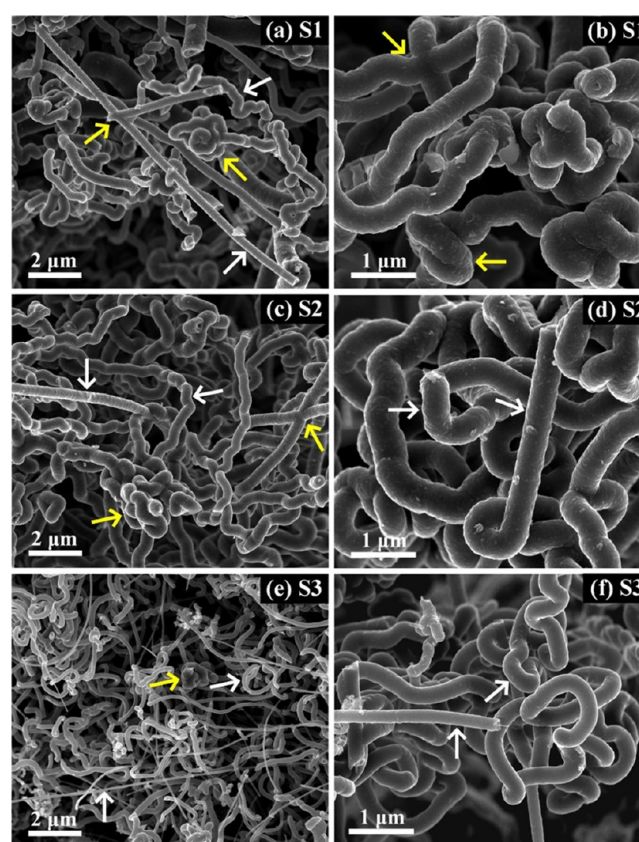

Figure 1. SEM images of N-CNS. (a,b) Sample S1, (c,d) Sample S2, and (e,f) Sample S3. The N-CNS contains predominantly entangled carbon nanofibers.

decomposition of propylene releases ethylene and methylene.[39] Previous studies have reported that water-assisted CVD favors the activity and lifetime of the catalysts,[42] while carbon monoxide promotes an increase in the yield production of carbon nanotubes.[46] Ethylene is also an efficient precursor to fabricate carbon nanotubes.[40,41] The considerable resemblance between carbon fibers of S1 and S2 is observed because isopropanol and ethanol molecules release ethylene and water during their thermal decomposition. The increment in the yield production in S3 could be due to the carbon monoxide released by the acetone. Besides, we observe that N-CNSs displayed hydrophobicity. A drop of water on the surface of S1 showed a quasi-spherical shape (see Figure SI-3). The real origin of the hydrophobicity of carbon sponge materials is a subject far from being clear, but the surface roughness and surface chemistry could be the keys to explain the hydrophobicity of carbon sponges. The interface between the drop of water and sponge could contain air bubbles because of the roughness of the sponge's surface,[47] and on the other hand, nonpolar functional groups anchored on the sponge's surface may repel water.[48] Therefore, the surface chemistry characterizations by X-ray photoelectron spectroscopy (XPS) and Fourier transform infrared spectroscopy (FTIR) could give us some insights into the nature of chemical species hosted on the surface of N-CNSs. We quantify the oxygen and nitrogen functional groups anchored on the surface of N-CNS. Functional groups with a hydrophobic feature such as ether groups (epoxy, methoxy, ethoxy, among others) could be the key to elucidate the possible scenarios of the hydrophobic property of N-CNSs, results are shown later.

Figures 2–4 depict the transmission electron microscopy (TEM) and high-resolution transmission electron microscopy
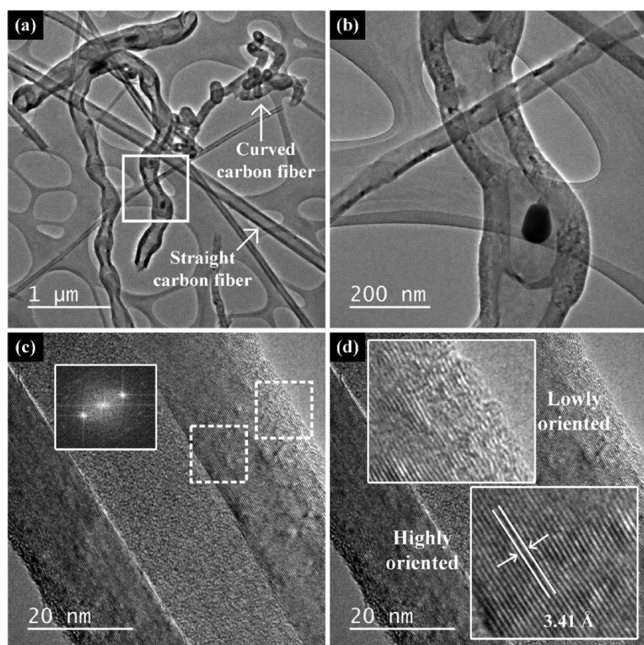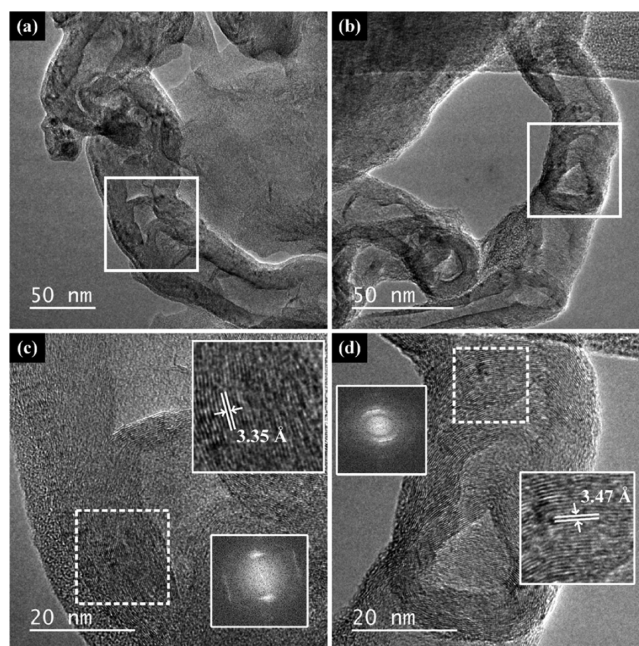

Figure 2. TEM images of N-CNS from sample S1. (a,b) Bamboo-type carbon nanotube with metallic Fe-based nanoparticles inside, (c) straight carbon nanotube, and (d) HRTEM images showing low and high ordered graphitic layers.
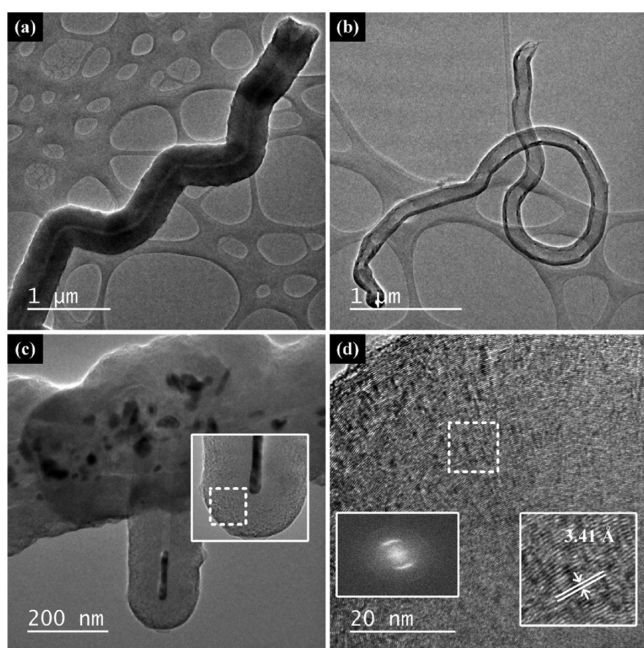
Figure 3. TEM images of N-CNS from sample S2. (a,b) Carbon fibers, (c) carbon fiber with Fe-based nanoparticles, and (d) HRTEM images showing the graphitic aspect of carbon fibers.

(HRTEM) images for S1, S2, and S3. Figure 2a shows the straight and curved carbon fiber, and a close-up image revealed clearly the curved fiber with bamboo segments and Fe-based nanoparticles inside (Figure 2b). Figure 2c depicts the HTERM image of multilayered straight carbon nanotubes with an interlayer distance of 0.341 nm. The interlayer distance


Figure 4. TEM images of N-CNS from sample S3. (a) Carbon nanotube with an irregular bamboo-shaped morphology and (b) high-magnification image from the square in (a) showing the graphitic layers. (c,d) Carbon nanotube showing the graphitic layers in different zones.

reported for carbon fiber with a turbostratic-type structure is 0.344 nm.[49] The core material of carbon nanotube showed well-aligned graphitic layers, whereas the outer more layers exhibited defected graphitic materials. Figure 3a,b depicts carbon fibers with different diameters in the absence of bamboo-shaped morphology. Figure 3c displays Fe-based nanoparticles inside the carbon fiber. An HRTEM image from S2 revealed an interlayer distance of 3.41 Å (Figure 3d). The carbon fiber showed a bamboo-shaped morphology, see Figure 4a,b. The interlayer distance depended strongly on the carbon fiber zone, the two zones analyzed yielded 3.35 and 3.47 Å, see Figure 4c,d.

Figure 5a–c displays the X-ray diffraction (XRD) plots showing the C(002) peaks, characteristic of graphitic materials. These peaks showed an asymmetry shape, which could be attributed to the existence of an expanded graphitic material (EGM). The asymmetric peaks were deconvoluted in two pseudo-Voigt curves and labeled γ- and π-curves, and Table SI-1 (Supporting Information) displays the details about the deconvolution analysis. The γ- and π-peak centers provide $d\gamma$ and $d\pi$ interlayer distances, respectively, where $d\gamma$ is attributed to the EGM while $d\pi$ refers to a well-ordered graphitic material. From this deconvolution analysis, the amount of EGM in N-CNSs exceeded 67%, reaching 81% for sample S1. Figure 5d depicts the XRD plot for $2\theta = 31-90°$, revealing the presence of peaks around $2\theta = 44$ and $54°$; however, these are not well defined. The presence of these unclear peaks is related to the small Fe-based nanoparticles. Figure 6 shows the thermogravimetric analysis (TGA) measurements for samples S1, S2, and S3. The TGA curves displayed two oxidative temperatures (T_1 and T_2), indicating the presence of two different carbon materials as also confirmed by the XRD characterizations. From TGA, it is clear that the three types of synthesized N-CNSs display different thermal stabilities, and
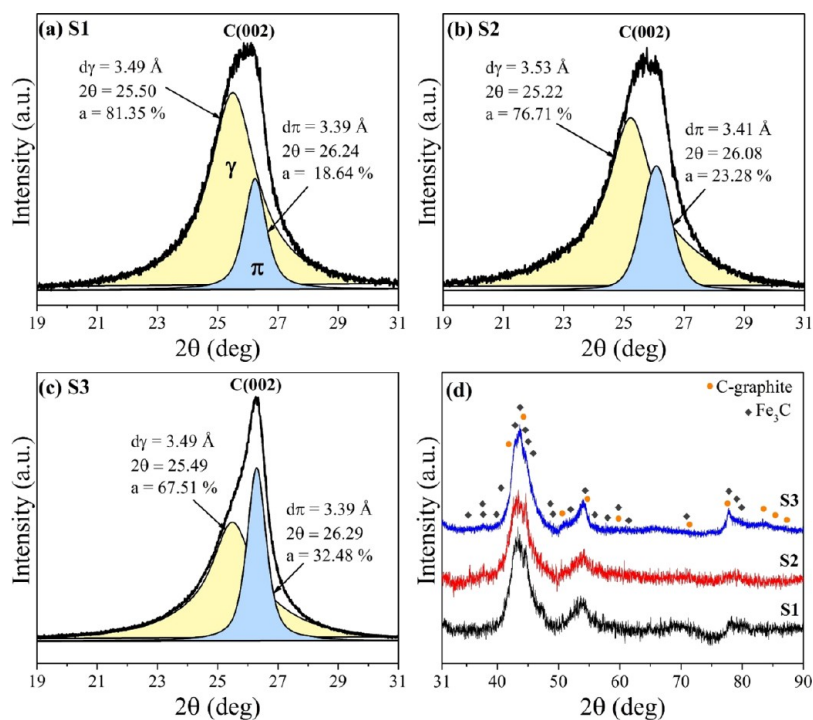
Figure 5. XRD plots for N-CNS. (a−c) Deconvolution analysis of the C(002) signal corresponding to the graphitic material. The deconvolution analysis was performed using two pseudo-Voigt curves; the γ- and π-curves refer to different graphitic materials. Table SI-1 displays the data derived from the deconvolution analysis. (d) XRD plots for $2\theta = 31-90°$, revealing the presence of iron-based nanoparticles, mainly Fe_3C (PDF 00-034-0001) and graphite (PDF 03-065-6212).
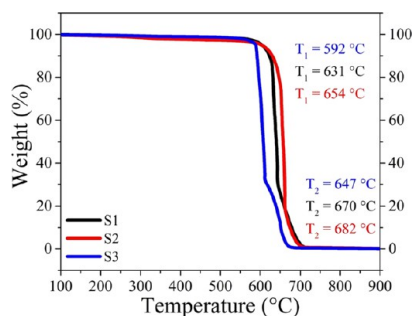

Figure 6. TGA curves for N-CNS. Results for samples S1 (isopropanol), S2 (isopropanol−ethanol), and S3 (isopropanol−acetone). Sample S1 showed the lowest oxidation temperature likely because of the small diameter of the carbon fiber.

those synthesized with isopropanol−acetone were the least thermally stable. In all cases, the remaining or residual materials were less than 0.5%.

Figure 7a displays the Raman spectroscopy analysis for N-CNSs. Here, the vertical lines correspond to the D- and G-peak bands, typical vibrational modes of graphite (D = 1350 cm^{-1} and G = 1580 cm^{-1}).[50,51] The carbon sponges showed downshifts of ∼7 cm^{-1} and ∼23 cm^{-1} for D- and G-bands, respectively. Notice that the ratio between the intensities of D- and G-peaks (I_D/I_G) provides information on the graphitization degree, and higher values of I_D/I_G indicate poor graphitization. We found that I_D/I_G is 0.80, 0.88, and 0.86 for samples S1, S2, S3, respectively. Therefore, samples synthesized with isopropanol−acetone or isopropanol−ethanol are less graphitic than those synthesized using only isopropanol. Deconvolution analysis of D- and G-peaks allows us to elucidate the different carbon species involved in the

carbon sponges. We used four Lorentzian curves to fit the profile peaks. Figure 7b−d displays the fitting of the peak profile for the D- and G-peaks. The Lorentzian curves were labeled D1-, D-, D2-, and G-peaks, and the results of the deconvolution are summarized in Table SI-2 (Supporting Information). The D1-peak is a signal attributed to graphite edges.[52,53] The D-peak corresponds to defects inside the carbon network, such as vacancies, doping, or nonhexagonal carbon rings.[54] The presence of the D2-peak could be assigned to C−C vibration modes of olefinic sp^2 groups, centered at ∼1510 cm^{-1}, as was reported by Ferrari and Robertson.[55]

The N-CNSs were characterized by XPS, revealing the presence C, N, O, and Si (see Figure SI-4). Interesting trends on the concentration of the involved chemical element were identified. The presence of silicon in the samples is attributed to the quartz tube where N-CNSs were grown. Usually, the N-CNSs displayed a high oxygen concentration above 5.4%. The N-CNSs synthesized with only isopropanol (sample S1) exhibited the highest oxygen concentration (9.2%). It is worth mentioning that oxygen abundance could be advantageous for many chemical applications.[56,57] Figures 8−10 display the deconvoluted high-resolution C 1s, N 1s, and O 1s peaks. The percentage of a chemical species can be estimated from the area under its corresponding curve in the deconvolution analysis. However, a pondered area (relative atomic ratio) by the atomic concentration derived from XPS survey provides a better estimation of the chemical groups involved in the entire sample. Tables SI-3−5 show the data on each curve, such as center, full width at half-maximum, area, and relative atomic ratio. For C 1s peaks, chemical species such as C−C, C=C, Fe−C, Si−C, C=O, and O−C=O were identified, see Figure 8a−c. Figure 8d displays the relative atomic ratios of carbon species for S1, S2, and S3. This
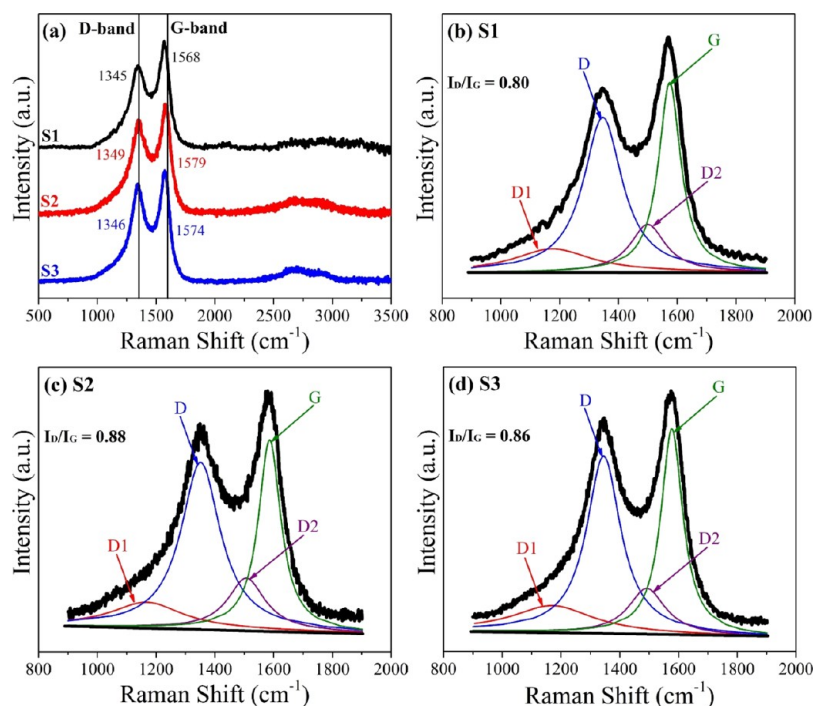
Figure 7. (a) Raman spectrum for N-CNS from samples S1, S2, and S3. All samples exhibited the typical D- and G-peaks of graphitic materials. The vertical lines in (a) refer to the vibration modes of graphite. (b−d) Deconvolution analysis of D- and G-band Raman peaks using four curves (D1, D, D2, and G). Table SI-2 displays the data from the deconvolution analysis.
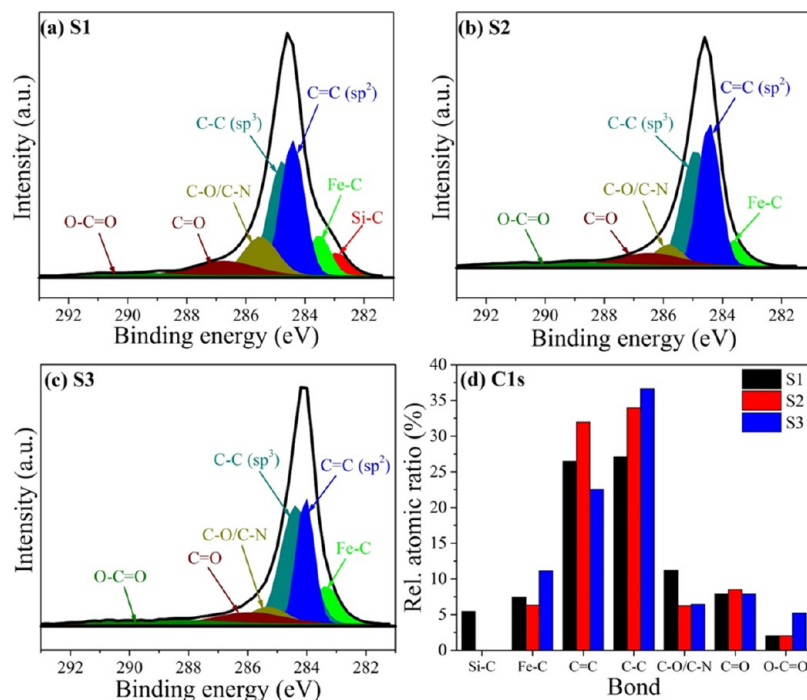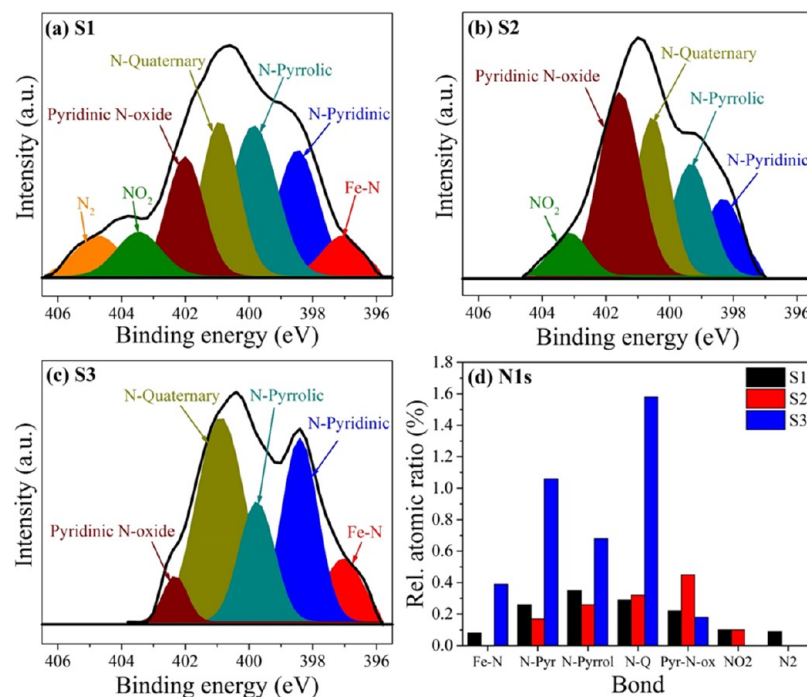

Figure 8. (a−c) Deconvoluted high-resolution C 1s XPS spectra for samples S1, S2, and S3. (d) Relative percentage for each chemical species calculated from the area under its corresponding curve. The deconvolution analysis shows that sp^2 (C=O) and sp^3 (C−O) dominate.

estimation revealed that the surface chemistry is mainly dominated by C−C and C=C bonds, which are related to sp^3- and sp^2-hybridized carbons, respectively. The highest percentage of sp^3 has been found for sample S3, which is related to carbon atoms linked to different chemical species, maybe due to the functional groups attached to carbon atoms placed at graphite edges or the defected graphitic material.

Raman characterizations revealed a well-defined D1 peak assigned to the defected graphitic material in sample S3 (edges, vacancies, and doping). Figure 9 displays the results for the high-resolution O 1s peaks. It has been found that C−O, O−C=O, C=O, and COOH species dominate the surface chemistry, which is assigned to ether, ester, quinone, and carboxylic functional groups, respectively. Because the N-CNSs
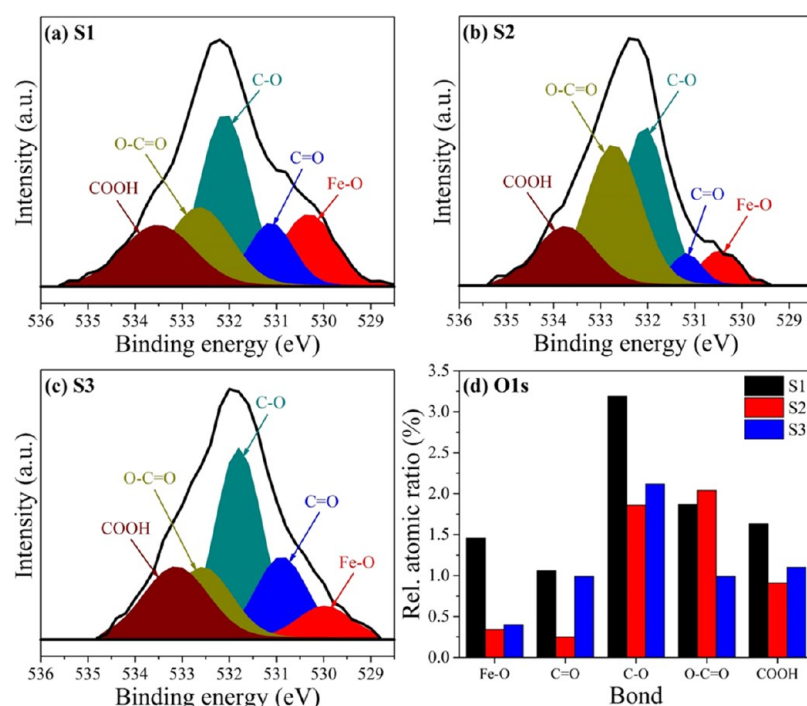
Figure 9. (a−c) Deconvoluted high-resolution O 1s XPS spectra for samples S1, S2, and S3. (d) Relative atomic ratio (%) for each chemical species. C=O is attributed to quinone, C−O ether groups, O−C=O ester groups, and COOH carboxylic. Sample S1 synthesized with only isopropanol showed a high percentage of ether group, which could be assigned to epoxy, methoxy, and ethoxy functional groups. Also, sample S1 exhibited the highest values of C=O and COOH attributed to quinone and carboxylic groups.

Figure 10. (a−c) Deconvoluted high-resolution N 1s XPS spectra for samples S1, S2, and S3. (d) Relative atomic ratio (%) for each chemical species. The main ways of incorporating the nitrogen in graphitic layers were identified. Sample S3 displayed a high relative atomic ratio for N-pyridinic, N-pyrrolic, and N-quaternary doping.

are hydrophobic, the C−O bond could be attributed to epoxy, methoxy, and ethoxy functional groups, whereas O−C=O is related to ethyl−ester functional group. The N-CNS surface rich in these functional groups would promote a hydrophobic surface as a result of a steric impediment. Notice that all these groups containing methyl groups in their tail are hydrophobic. However, more investigation is needed to elucidate the chemical functional groups involved at the surface of N-CNSs. The relative atomic ratio (%) of these functional groups is displayed in Figure 9d. High-resolution deconvoluted N 1s

peaks are shown in Figure 10. The relative atomic ratio of different nitrogen species can be seen in Figure 10d. In all samples, we found N-pyridinic, N-pyrrolic, N-quaternary, and pyridinic N-oxide species. Sample S3 showed the highest values for almost all nitrogen species. We also performed FTIR characterizations of N-CNSs (Figure 11). The vibration modes
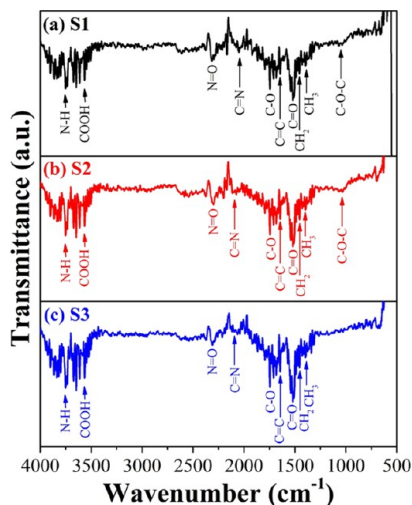

Figure 11. FTIR spectra of N-CNS. Results for samples (a) S1 (isopropanol), (b) S2 (isopropanol−ethanol), and (c) S3 (isopropanol−acetone). The signal of C−O−C at 1055 cm^{-1} is identified only for S1 and S2 samples.

corresponding to C=C sp^2 ≈ 1650 cm^{-1} (graphitic material) were detected. The aliphatic CH$_2$ ~1450 cm^{-1} and CH$_3$ ~1390 cm^{-1} were also present. The vibrational modes of C=O bonds related to ester functional groups appeared at ~1749 cm^{-1}. The nitrogen bond signals for C=N at 2055 cm^{-1} and N=O 2313 cm^{-1} were also identified, besides the fact that the vibrational modes of N−H of amine groups are present at 3750 cm^{-1}. Table SI-6 displays the vibrational models for the different bonds illustrated in FTIR spectra.

The absorption properties were measured for gasoline, methanol, diesel, vacuum oil, vegetable oil, ethylene glycol, and dichlorobenzene. For each solvent and type of N-CNSs, a

piece of ~1 cm length (Figure 12a) was selected, which was immersed for 5 min, see Figure 12b,c. Subsequently, the N-CNS was taken out from the solvent and immediately weighed. Finally, the N-CNS was burnt to remove the organic solvent (see Figure 12d). The weight after burning was compared with the initial weight (before the immersion); it was found that these values were similar. Then, the same sponge was reused, yielding similar values of the absorption capacity for that obtained for the pristine sponge. Figure 12e−g displays the absorption capacity (Q) for S1, S2, and S3. The highest values of Q were obtained for S1, followed by S2 and S3. This trend could be explained in terms of surface chemistry.[49] From XPS characterizations, S1 showed the highest oxygen concentration with a significant contribution of methoxy, ethoxy, and ester functional groups. The high concentration of these groups with a methyl tail makes sample S1 efficient for the absorption of organic solvents. Because S2 and S3 revealed a similar oxygen concentration according to XPS characterizations, one would expect similar absorption properties; however, S2 was better than S3. This fact could be likely due to the higher presence of ester functional groups in S2 (see Figure 9d). The values of Q obtained for our sponges are competitive with other CNSs synthesized using other alcohol precursors in a CVD experiment.[2,36,37] However, these are an order of magnitude less than those CNSs produced using dichlorobenzene as a precursor.[1]

Figure 13a−c shows the results of cyclic voltammetry for N-CNSs, revealing a well-defined redox process. The peak position, peak shape, and peak intensity of the anodic and cathodic currents depended on the type of N-CNSs, see Table 2. The anodic and cathodic current intensities were higher for S1 than for S3 and S2 regardless of the scan rate (Figure SI-5). This fact could be related to the high quinone, carboxylic, and ester functional group concentrations displayed by sample S1. In Figure 14, we proposed a possible mechanism in the redox process involving the quinone, carboxylic, and ethyl−ester functional groups. Table 2 displays the potential difference between the anodic and cathodic peaks (ΔE_p). As it is expected, ΔE_p increases as the scan rate increases, and it was observed that $\Delta E_p(S1) > \Delta E_p(S3) > \Delta E_p(S2)$. Similarly, the intensity of the anodic current shows the following behavior Ia(S1) > Ia(S3) > Ia(S2). The different behavior observed for
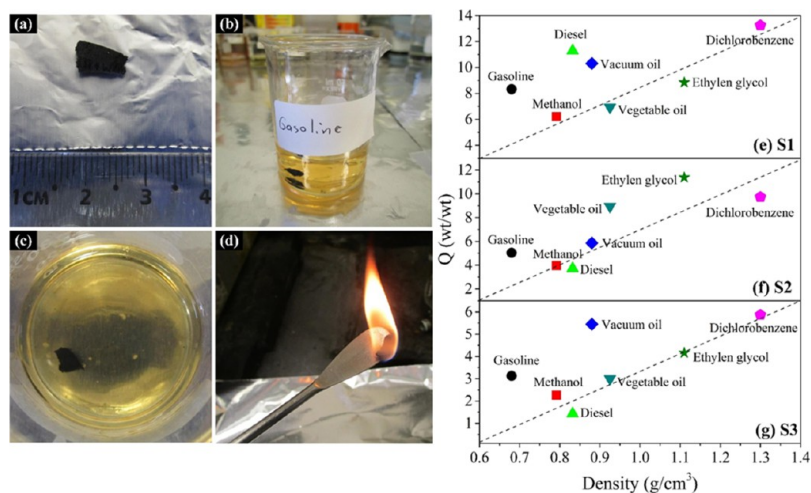
Figure 12. (a) Photography of N-CNS. (b,c) Sponge immersed in gasoline for 5 min and is subsequently burnt to remove the solvent. The burnt sponge is reusable. The absorption capacity (Q) was obtained from $Q = Q_f/Q_0$. (e−g) Values of Q as a function of solvent density.
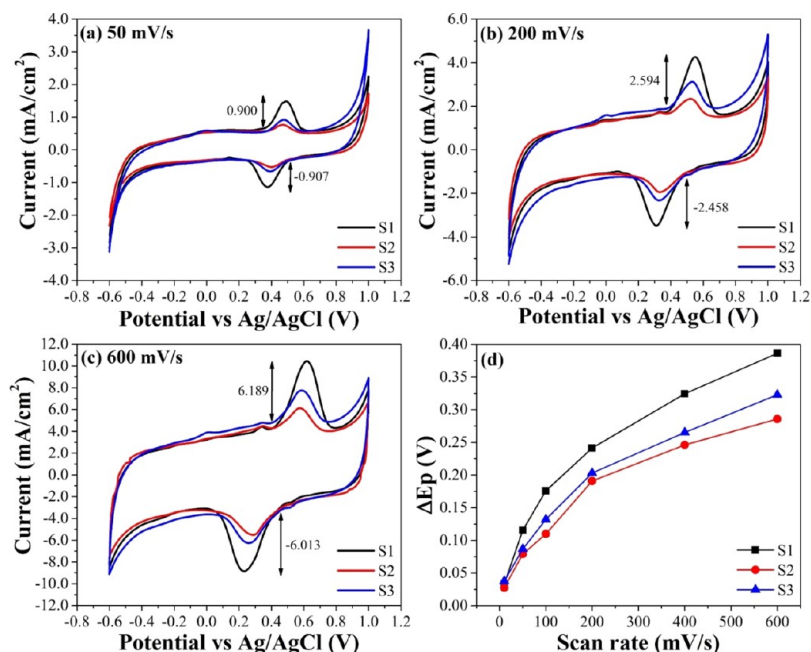
Figure 13. Cycle voltammetry of N-CNS electrode in 0.5 M H$_2$SO$_4$ aqueous solution. Results for SI, S2, and S3 samples in different scan rates: (a) 50 mV/s, (b) 200 mV/s, and (c) 600 mV/s. (d) Potential differences between anodic and cathodic peaks (ΔEp). Sample S1 synthesized with only isopropanol displayed the highest anodic and cathodic currents. The lowest values of ΔEp were obtained for sample S3 synthesized with isopropanol–acetone.

Table 1. Content of Chemical Precursors at Solutions Used in the AACVD Experiment[a,b]

S-BTF	(wt %)	S-I	(wt %)
benzylamine	97.0	**isopropanol**	98.5
ferrocene	2.5	ferrocene	1.25
thiophene	0.5	thiophene	0.125
S-IE	(wt %)	S-IA	(wt %)
isopropanol–ethanol (1:1)	98.5	**isopropanol–acetone (1:1)**	98.5
ferrocene	1.25	ferrocene	1.25
thiophene	0.125	thiophene	0.125

[a]In all experiments, the content of sprayer-A (S-BTF) was not changed. The content of sprayer-B was changed with S-I, S-IE, and S-IA solutions to synthesize sample S1, S2, and S3, respectively. [b]500 mL was prepared for each solution.

ΔE_p and Ia could be qualitatively understood in terms of the percentage estimation of functional groups involved in the surface of N-CNSs. The high concentration of quinone and carboxylic groups in S1 could be responsible for the high value of Ia where the redox process could be carried out via quinone, carboxylic, and ethyl–ester groups. Notice that a low relative atomic ratio of quinone and carboxylic groups in S2 originated low Ia values. Furthermore, the low values of ΔE_p in S2 could be correlated with the high concentration of pyridinic N-oxide. From electrochemical measurements, it is clear that the surface chemistry is different in all N-CNSs as also demonstrated by XPS characterizations.

Figure 15 depicts the magnetic hysteresis loops for N-CNSs at room temperature (300 K). Results showed that the N-CNSs exhibit a ferromagnetic behavior because of the iron-based catalytic particle inside the graphitic material. The magnetization measurements were carried out in a field range of ±20 kOe. Magnetic hysteresis loops are shown in the range of ±8 kOe for better visualization. The corresponding saturation magnetization (M_s), coercive field (H_c), and remanence (M_r) are indicated. M_s was sensitive to the type of N-CNSs, and their values were below 6×10^{-4} emu. Sample S1 revealed the most significant values of M_s, followed by sample S3. H_c reached values up to ~0.29 kOe slightly higher than those found for α-Fe or Fe$_3$C nanoparticles inside multiwalled carbon nanotubes.[58–60] Previous results on the magnetic properties of carbon nanotubes with Fe$_2$O$_3$ (maghemite) and Fe$_3$C (cementite) inside reported an M_s of

Table 2. Data from Cyclic Voltammetry Measurements with Different Scan Rates for Samples S1, S2, and S3[a]

	S1			S2			S3		
scan rate (mV/s)	anodic	cathodic	ΔE_p (V)	anodic	cathodic	ΔE_p (V)	anodic	cathodic	ΔE_p (V)
10	0.4513	0.4180	0.0333	0.4481	0.4206	0.0275	0.4541	0.4165	0.0376
50	0.4913	0.3758	0.1155	0.4728	0.3938	0.0790	0.4773	0.3904	0.0869
100	0.5205	0.3446	0.1759	0.4876	0.3777	0.1099	0.4988	0.3668	0.1320
200	0.5499	0.3086	0.2413	0.5230	0.3319	0.1911	0.5315	0.3282	0.2032
400	0.5906	0.2662	0.3244	0.5539	0.3078	0.2461	0.5595	0.2943	0.2652
600	0.6177	0.2313	0.3864	0.5773	0.2881	0.2892	0.5834	0.2606	0.3228

[a]Results for voltages where the anodic and cathodic peaks occur. Potential differences between the anodic and cathodic peaks (ΔEp).
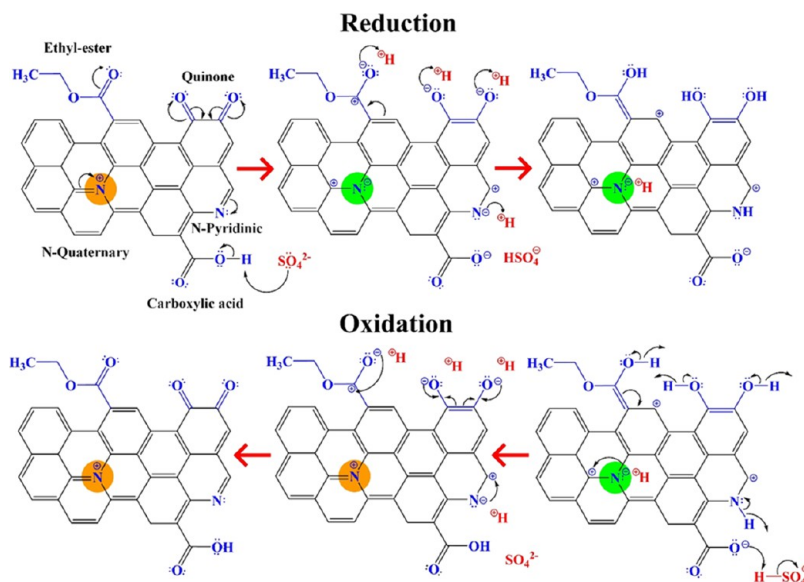
Figure 14. Functional groups that could participate in the redox process. For the reduction process, these groups are protonated, whereas in the oxidation process, these are deprotonated.
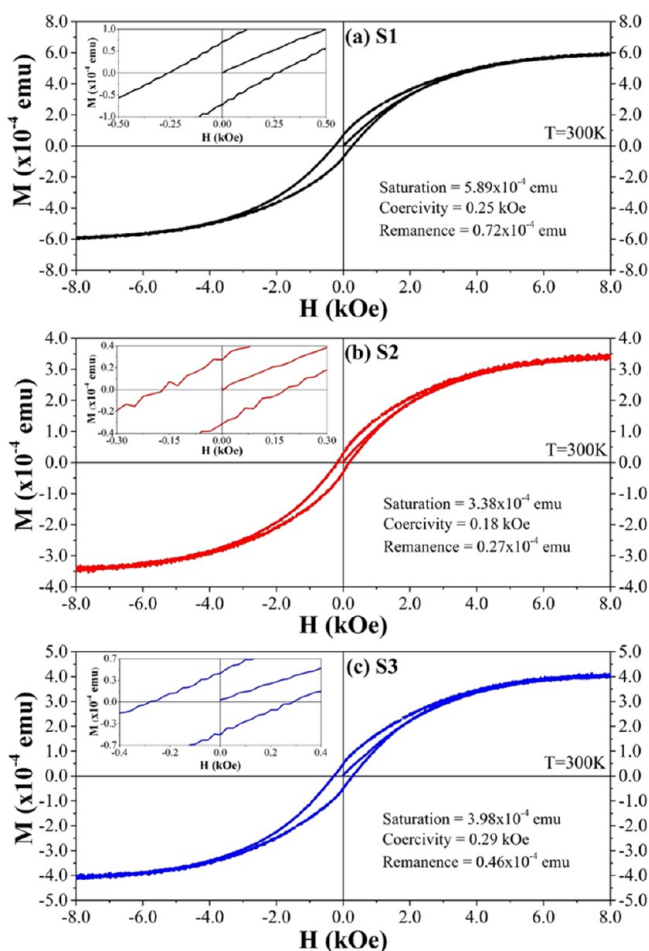
Figure 15. Magnetic hysteresis loops of N-CNS measured at 300 K. (a) S1 (isopropanol), (b) S2 (isopropanol−ethanol), and (c) S3 (isopropanol−acetone). The magnetic measurements were carried out at 300 K. The coercive field was 0.25, 0.18, and 0.29 kOe for samples S1, S2, and S3, respectively.

5 emu/g and an H_c of ∼500 Oe.[61] The ferromagnetism displayed by N-CNSs could be useful for several applications such as magnetic sensor devices, stem cell transplantation, and magnetic fluid hyperthermia.

3. CONCLUSIONS

We have fabricated N-CNSs by AACVD method using isopropanol-based mixture, benzylamine, ferrocene, and thiophene as precursors. We used isopropanol-based mixture as precursors: isopropanol, isopropanol−ethanol (1:1), and isopropanol−acetone (1:1). On the basis of our investigations, we remark five crucial points: (1) According to the XPS characterizations, the N-CNSs synthesized using only iso-propanol displayed a superoxygenated sponge. (2) The N-CNSs produced with isopropanol revealed a high concen-tration of ether groups (C−O), which could be attributed to methoxy, ethoxy, phenols, epoxy, and possibly to complex oxygenated large carbon chains anchored on the surface of carbon sponge. (3) The N-CNSs produced using only isopropanol displayed the highest anodic and cathodic currents, confirming the importance of oxygen functionaliza-tion in the electroactivity of graphitic materials. (4) The surface chemistry of our sponges was explored and correlated with the chemical−physical properties such as hydrophobicity, electroactivity, and absorption capacity. (5) Our work provides an alternative route to synthesize in situ functionalized graphitic materials. In most cases, the oxygen functionalization of carbon material requires aggressive acid treatments per hour and tedious and long-time consumer methods to remove the acidity. Magnetic measurements at room temperature revealed that N-CNSs are ferromagnetic with high coercive fields. In summary, we have synthesized multifunctional materials with outstanding superhydrophobic, oil-absorbent, electroactive, and ferromagnetic properties. We envisage that our N-CNSs could be applied in lithium-ion batteries, oil removal in spills, magnetic sensors, among others. However, more surface chemistry and applications of N-CNSs deserve to be more deeply investigated.

4. EXPERIMENTAL DETAILS

The N-CNSs were produced using a modified AACVD method, as was used elsewhere.[36,37] Figure SI-6 (Supporting Information) displays a schematic representation of the experimental setup. Briefly, the AACVD system consists of two independent sprayers (sprayer-A and sprayer-B) connected by a Y-glass adapter to a quartz tube (length: 90 cm; diameter: 2.5 cm) placed inside a tubular furnace (Barnstead Thermolyne Mod. F21135). The quartz tube is connected to a condenser and an acetone trap for residuals. A solution made of benzylamine (Sigma-Aldrich, 99.00%), ferrocene (Sigma-Aldrich, 98.00%), and thiophene (Sigma-Aldrich, 99.00%) is fixed in sprayer-A, whereas another solution containing isopropanol-based mixture, ferrocene, and thiophene is set in sprayer-B. In this case, three different solutions were considered: (i) isopropanol only (CTR Scientific, 99.50%), (ii) isopropanol−ethanol 1:1 (CTR Scientific, 96.50%), and (iii) isopropanol−acetone 1:1 (CTR Scientific, 99.95%). The solution in sprayer-A was named S-BFT. The solutions used in sprayer-B were named S-I (containing only isopropanol), S-IE (containing isopropanol and ethanol), and S-IA (containing isopropanol and acetone). Table 1 summarizes the chemical precursors and concentrations used in each experiment. Thus, N-CNSs labeled S1, S2, and S3 were produced using S-I, S-IE, and S-IA, respectively. The nebulized precursors formed inside the sprayers were transported to the quartz tube reactor by two different gas flows. In sprayer-A, a mixture of Ar/H_2 (Infra, 95/5%) at 1.0 L/min was employed. In sprayer-B, the gas used was Ar (Infra, 99.999%) at 0.8 L/min. The temperature of synthesis was 1020 °C for 4 h. The CNS-type nanomaterial obtained was collected inside the quartz tube using a stained steel rod. Samples grown in the central part of the tubular furnace were characterized by SEM (FEI-Helios NanoLab DualBeam 600 Microscopy), HRTEM (FEI Tecnai F30), Raman spectroscopy (Micro-Raman Renishaw) using a power laser beam of 532 nm (2.33 eV), TGA (STA 6000 PerkinElmer), XRD (SmartLab X-ray Diffractometer, Rigaku, Co.) using a power source of Cu (Kα = 1.54 Å), and XPS (PHI 5000 VersaProbe II). For FTIR characterizations, the samples were prepared with KBr (Sigma-Aldrich, FT-IR grade ≥99%). An equivalent weight of 0.2% of N-CNSs deposited in an agate mortar was milled, and then an equivalent weight of 99.8% of KBr was added and incorporated using the agate pestle. The FTIR spectra were collected by Thermo-Fisher Nicolet 6700 equipment at 128 scan with an attenuated total reflection tip. The adsorption test of oil and organic solvents was realized by weighing an N-CNS (S = 1−3) sample (Q_0), the sample was immersed in oil or organic solvent for 5 min, then the sample was put in a wax paper for few seconds to clean the excess of solvent, and then the sponge was weighed again (Q_f). The absorption capacity was defined using the next relation $Q = Q_f/Q_0$, where Q is the capacity of absorption expressed as a dimensionless quantity. Cycles of voltammetry of N-CNSs were measured with varying scan rates (10, 50, 100, 200, 400, and 600 mV/s) with a potential window of −0.8−1.2 V using VSP 300 multichannel potentiostat (BioLogic Science Instrument). An Ag/AgCl/saturated KCl reference electrode (Mod RE 1-CP) and the counter electrode of platinum were used. The working electrode was prepared using a 904L stainless steel wire mesh (50 mesh, Hebei Hao Cheng Metal Wire Mesh). A sample of CNS with ~1.0 cm² of the area was held using the wire mesh. Finally, the reference, counter, and working electrodes were immersed in sulfuric acid (0.5 M) as electrolyte (pH = 0.5) at room temperature. Magnetic characterization of the CNSs was done using a physical property measurement system (DynaCool, Quantum Design). The magnetic hysteresis loops were measured at room temperature (300 K), and the magnetic fields were in the range of ±20 kOe.

■ ASSOCIATED CONTENT

Ⓢ Supporting Information

The Supporting Information is available free of charge on the ACS Publications website at DOI: 10.1021/acsomega.9b01773.

> Data from the deconvolution analysis of the XRD pattern for the (002) graphitic peak; data from the deconvolution analysis of D- and G-Raman peaks; data from the deconvolution analysis of C 1s, N 1s, and O 1s XPS spectra ; SEM images of backscattered electron and EDS of N-CNSs; diameter distribution of N-CNSs; photograph of drops of water on the surface of N-CNSs; XPS survey plots for N-CNSs; anodic current plot as a function of the scan rate for N-CNSs; and schematic representation of the experimental setup (PDF)

■ AUTHOR INFORMATION

Corresponding Author

*E-mail: flo@ipicyt.edu.mx.

ORCID ⓘ

Alejandro J. Cortés-López: 0000-0002-6467-4595
Emilio Muñoz-Sandoval: 0000-0002-6095-4119
Florentino López-Urías: 0000-0003-4001-0038

Notes

The authors declare no competing financial interest.

■ REFERENCES

(1) Gui, X.; Wei, J.; Wang, K.; Cao, A.; Zhu, H.; Jia, Y.; Shu, Q.; Wu, D. Carbon Nanotube Sponges. *Adv. Mater.* **2010**, *22*, 617−621.

(2) Muñoz-Sandoval, E.; Cortes-López, A. J.; Flores-Gómez, B.; Fajardo-Díaz, J. L.; Sánchez-Salas, R.; López-Urías, F. Carbon sponge-type nanostructures based on coaxial nitrogen-doped multiwalled carbon nanotubes grown by CVD using benzylamine as precursor. *Carbon* **2017**, *115*, 409−421.

(3) Wang, L.; Wang, X.; Zhou, J.-B.; Zhao, R.-S. Carbon nanotube sponges as a solid-phase extraction adsorbent for the enrichment and determination of polychlorinated biphenyls at trace levels in environmental water samples. *Talanta* **2016**, *160*, 79−85.

(4) Dai, Z.; Liu, L.; Qi, X.; Kuang, J.; Wei, Y.; Zhu, H.; Zhang, Z. Three-dimensional Sponges with Super Mechanical Stability: Harnessing True Elasticity of Individual Carbon Nanotubes in Macroscopic Architectures. *Sci. Rep.* **2015**, *6*, 18930.

(5) Zhao, W.; Li, Y.; Wang, S.; He, X.; Shang, Y.; Peng, Q.; Wang, C.; Du, S.; Gui, X.; Yang, Y.; Yuan, Q.; Shi, E.; Wu, S.; Xu, W.; Cao,

A. Elastic improvement of carbon nanotube sponges by depositing amorphous carbon coating. *Carbon* **2014**, *76*, 19−26.

(6) Zhao, W.; Shan, C.; Elias, A. L.; Rajukumar, L. P.; O'Brien, D. J.; Terrones, M.; Wei, B.; Suhr, J.; Lu, X. L. Hyperelasticity of three-dimensional carbon nanotube sponge controlled by the stiffness of covalent junctions. *Carbon* **2015**, *95*, 640−645.

(7) Shan, C.; Zhao, W.; Lu, X. L.; O'Brien, D. J.; Li, Y.; Cao, Z.; Elias, A. L.; Cruz-Silva, R.; Terrones, M.; Wei, B.; Suhr, J. Three-Dimensional Nitrogen-Doped Multiwall Carbon Nanotube Sponges with Tunable Properties. *Nano Lett.* **2013**, *13*, 5514−5520.

(8) Chen, J.; Gui, X.; Wang, Z.; Li, Z.; Xiang, R.; Wang, K.; Wu, D.; Xia, X.; Zhou, Y.; Wang, Q.; Tang, Z.; Chen, L. Superlow Thermal Conductivity 3D Carbon Nanotube Network for Thermoelectric Applications. *ACS Appl. Mater. Interfaces* **2012**, *4*, 81−86.

(9) Gui, X.; Zeng, Z.; Zhu, Y.; Li, H.; Lin, Z.; Gan, Q.; Xiang, R.; Cao, A.; Tang, Z. Three-Dimensional Carbon Nanotube Sponge-Array Architectures with High Energy Dissipation. *Adv. Mater.* **2014**, *26*, 1248−1253.

(10) Li, H.; Gui, X.; Zhang, L.; Wang, S.; Ji, C.; Wei, J.; Wang, K.; Zhu, H.; Wu, D.; Cao, A. Carbon nanotube sponge filters for trapping nanoparticles and dye molecules from water. *Chem. Commun.* **2010**, *46*, 7966−7968.

(11) Gao, Y.; Zhou, Y. S.; Xiong, W.; Wang, M.; Fan, L.; Rabiee-Golgir, H.; Jiang, L.; Hou, W.; Huang, X.; Jiang, L.; Silvain, J.-F.; Lu, Y. F. Highly Efficient and Recyclable Carbon Soot Sponge for Oil Cleanup. *ACS Appl. Mater. Interfaces* **2014**, *6*, 5924−5929.

(12) Li, X.; Xue, Y.; Zou, M.; Zhang, D.; Cao, A.; Duan, H. Direct Oil Recovery from Saturated Carbon Nanotube Sponges. *ACS Appl. Mater. Interfaces* **2016**, *8*, 12337−12343.

(13) Zhu, K.; Shang, Y.-Y.; Sun, P.-Z.; Li, Z.; Li, X.-M.; Wei, J.-Q.; Wang, K.-L.; Wu, D.-H.; Cao, A.-Y.; Zhu, H.-W. Oil spill cleanup from sea water by carbon nanotube sponges. *Front. Mater. Sci.* **2013**, *7*, 170−176.

(14) Camilli, L.; Pisani, C.; Gautron, E.; Scarselli, M.; Castrucci, P.; D'Orazio, F.; Passacantando, M.; Moscone, D.; De Crescenzi, M. A three-dimensional carbon nanotube network for water treatment. *Nanotechnology* **2014**, *25*, 065701.

(15) Li, H.; Gui, X.; Zhang, L.; Ji, C.; Zhang, Y.; Sun, P.; Wei, J.; Wang, K.; Zhu, H.; Wu, D.; Cao, A. Enhanced Transport of Nanoparticles Across a Porous Nanotube Sponge. *Adv. Funct. Mater.* **2011**, *21*, 3439−3445.

(16) Jiang, H.; Lee, P. S.; Li, C. 3D carbon based nanostructures for advanced supercapacitors. *Energy Environ. Sci.* **2013**, *6*, 41−53.

(17) Qie, L.; Chen, W.; Xu, H.; Xiong, X.; Jiang, Y.; Zou, F.; Hu, X.; Xin, Y.; Zhang, Z.; Huang, Y. Synthesis of functionalized 3D hierarchical porous carbon for high-performance supercapacitors. *Energy Environ. Sci.* **2013**, *6*, 2497−2504.

(18) Zhong, J.; Yang, Z.; Mukherjee, R.; Varghese Thomas, A.; Zhu, K.; Sun, P.; Lian, J.; Zhu, H.; Koratkar, N. Carbon nanotube sponges as conductive networks for supercapacitor devices. *Nano Energy* **2013**, *2*, 1025−1030.

(19) Erbay, C.; Yang, G.; De Figueiredo, P.; Sadr, R.; Yu, C.; Han, A. Three-dimensional porous carbon nanotube sponges for high-performance anodes of microbial fuel cells. *J. Power Sources* **2015**, *298*, 177−183.

(20) Chen, J.; Meng, F.; Gui, X.; Sun, H.; Zeng, Z.; Li, Z.; Zhou, Y.; Tang, Z. The application of a three dimensional CNT-sponge as the counter electrode for dye-sensitized solar cells. *Carbon* **2012**, *50*, 5618−5630.

(21) Shen, Y.; Sun, D.; Yu, L.; Zhang, W.; Shang, Y.; Tang, H.; Wu, J.; Cao, A.; Huang, Y. A high-capacity lithium-air battery with Pd modified carbon nanotube sponge cathode working in regular air. *Carbon* **2013**, *62*, 288−295.

(22) Wang, L.; Wang, M.; Huang, Z.-H.; Cui, T.; Gui, X.; Kang, F.; Wang, K.; Wu, D. Capacitive deionization of NaCl solutions using carbon nanotube sponge electrodes. *J. Mater. Chem.* **2011**, *21*, 18295−18299.

(23) Correa-Duarte, M. A.; Wagner, N.; Rojas-Chapana, J.; Morsczeck, C.; Thie, M.; Giersig, M. Fabrication and Biocompatibility of Carbon Nanotube-Based 3D Networks as Scaffolds for Cell Seeding and Growth. *Nano Lett.* **2004**, *4*, 2233−2236.

(24) Hou, X.; Choy, K.-L. Processing and Applications of Aerosol-Assisted Chemical Vapor Deposition. *Chem. Vap. Deposition* **2006**, *12*, 583−596.

(25) Kumar, M.; Ando, Y. Chemical Vapor Deposition of Carbon Nanotubes: A Review on Growth Mechanism and Mass Production. *J. Nanosci. Nanotechnol.* **2010**, *10*, 3739−3758.

(26) Gui, X.; Zeng, Z.; Lin, Z.; Gan, Q.; Xiang, R.; Zhu, Y.; Cao, A.; Tang, Z. Magnetic and Highly Recyclable Macroporous Carbon Nanotubes for Spilled Oil Sorption and Separation. *ACS Appl. Mater. Interfaces* **2013**, *5*, 5845−5850.

(27) Zhao, W.; Shan, C.; Elias, A. L.; Rajukumar, L. P.; O'Brien, D. J.; Terrones, M.; Wei, B.; Suhr, J.; Lu, X. L. Hyperelasticity of three-dimensional carbon nanotube sponge controlled by the stiffness of covalent junctions. *Carbon* **2015**, *95*, 640−645.

(28) Hashim, D. P.; Narayanan, N. T.; Romo-Herrera, J. M.; Cullen, D. A.; Hahm, M. G.; Lezzi, P.; Suttle, J. R.; Kelkhoff, D.; Muñoz-Sandoval, E.; Ganguli, S.; Roy, A. R.; Smith, D. J.; Vajtai, R.; Sumpter, B. G.; Meunier, V.; Terrones, H.; Terrones, M.; Ajayan, P. M. Covalently bonded three-dimensional carbon nanotube solids via boron induced nanojunctions. *Sci. Rep.* **2012**, *2*, 363.

(29) Grüneis, A.; Rümmeli, M. H.; Kramberger, C.; Barreiro, A.; Pichler, T.; Pfeiffer, R.; Kuzmany, H.; Gemming, T.; Büchner, B. High quality double wall carbon nanotubes with a defined diameter distribution by chemical vapor deposition from alcohol. *Carbon* **2006**, *44*, 3177−3182.

(30) Huang, L.; Cui, X.; White, B.; O'Brien, S. P. Long and Oriented Single-Walled Carbon Nanotubes Grown by Ethanol Chemical Vapor Deposition. *J. Phys. Chem. B* **2004**, *108*, 16451−16456.

(31) Botello-Méndez, A.; Campos-Delgado, J.; Morelos-Gómez, A.; Romo-Herrera, J. M.; Rodríguez, Á. G.; Navarro, H.; Vidal, M. A.; Terrones, H.; Terrones, M. Controlling the dimensions, reactivity and crystallinity of multiwalled carbon nanotubes using low ethanol concentrations. *Chem. Phys. Lett.* **2008**, *453*, 55−61.

(32) Peng, X.; Koczkur, K.; Chen, A. Synthesis of well-aligned bamboo-like carbon nanotube arrays from ethanol and acetone. *J. Phys. D: Appl. Phys.* **2008**, *41*, 095409.

(33) Zhu, J.; Jia, J.; Kwong, F.-l.; Ng, D. H. L. Synthesis of bamboo-like carbon nanotubes on a copper foil by catalytic chemical vapor deposition from ethanol. *Carbon* **2012**, *50*, 2504−2512.

(34) Qi, H.; Qian, C.; Liu, J. Synthesis of High-Purity Few-Walled Carbon Nanotubes from Ethanol/Methanol Mixture. *Chem. Mater.* **2006**, *18*, 5691−5695.

(35) Li, Y.-L.; Zhang, L.-H.; Zhong, X.-H.; Windle, A. H. Synthesis of high purity single-walled carbon nanotubes from ethanol by catalytic gas flow CVD reactions. *Nanotechnology* **2007**, *18*, 225604.

(36) Muñoz-Sandoval, E.; Fajardo-Díaz, J. L.; Sánchez-Salas, R.; Cortés-López, A. J.; López-Urías, F. Two Sprayer CVD Synthesis of Nitrogen-doped Carbon Sponge-type Nanomaterials. *Sci. Rep.* **2018**, *8*, 2983.

(37) Cortés-López, A. J.; Muñoz-Sandoval, E.; López-Urías, F. Efficient carbon nanotube sponges production boosted by acetone in CVD-Synthesis. *Carbon* **2018**, *135*, 145−156.

(38) Trenwith, A. B. Thermal decomposition of isopropanol. *J. Chem. Soc., Faraday Trans.* **1975**, *71*, 2405−2412.

(39) Hung, W.-C.; Tsai, C.-Y.; Matsui, H.; Wang, N.-S.; Miyoshi, A. Experimental and Theoretical Study on the Thermal Decomposition of C3H6 (Propene). *J. Phys. Chem. A* **2015**, *119*, 1229−1237.

(40) Zhang, Q.; Huang, J.-Q.; Zhao, M.-Q.; Qian, W.-Z.; Wang, Y.; Wei, F. Radial growth of vertically aligned carbon nanotube arrays from ethylene on ceramic spheres. *Carbon* **2008**, *46*, 1152−1158.

(41) Yuan, L.; Saito, K.; Hu, W.; Chen, Z. Ethylene flame synthesis of well-aligned multi-walled carbon nanotubes. *Chem. Phys. Lett.* **2001**, *346*, 23−28.

(42) Hata, K.; Fubata, D. N.; Mizuno, K.; Namai, T.; Yumura, M.; Iijima, S. Water-Assisted Highly Efficient Synthesis of Impurity-Free Single-Walled Carbon Nanotubes. *Science* **2004**, *306*, 1362−1364.

(43) Bettinger, H. F. Effects of Finite Carbon Nanotube Length on Sidewall Addition of Fluorine Atom and Methylene. *Org. Lett.* **2004**, *6*, 731−734.

(44) Wu, C.-W.; Matsui, H.; Wang, N.-S.; Lin, M. C. Shock Tube Study on the Thermal Decomposition of Ethanol. *J. Phys. Chem. A* **2011**, *115*, 8086.

(45) Smith, J. R. E.; Hinshelwood, C. N. The thermal decomposition of acetone. *Proc. R. Soc. London, Ser. A* **1994**, *183*, 33−37.

(46) Nikolaev, P.; Bronikowski, M. J.; Bradley, R. K.; Rohmund, F.; Colbert, D. T.; Smith, K. A.; Smalley, R. E. Gas-phase catalytic growth of single-walled carbon nanotubes from carbon monoxide. *Chem. Phys. Lett.* **1999**, *313*, 91−97.

(47) Porcheron, F.; Monson, P. A. Mean-Field Theory of Liquid Droplets on Roughened Solid Surfaces: Application to Super-hydrophobicity. *Langmuir* **2006**, *22*, 1595−1601.

(48) Chi, F.-H.; Amy, G. L. Kinetic study on the sorption of dissolved natural organic matter onto different aquifer materials: the effects of hydrophobicity and functional groups. *J. Colloid Interface Sci.* **2004**, *274*, 380−391.

(49) Saito, Y.; Yoshikawa, T.; Bandow, S.; Tomita, M.; Hayashi, T. Interlayer spacings in carbon nanotubes. *Phys. Rev. B: Condens. Matter Mater. Phys.* **1993**, *48*, 1907−1909.

(50) Dresselhaus, M. S.; Dresselhaus, G.; Saito, R.; Jorio, A. Raman spectroscopy of carbon nanotubes. *Phys. Rep.* **2005**, *409*, 47−99.

(51) Ferrari, A. C.; Meyer, J. C.; Scardaci, V.; Casiraghi, C.; Lazzeri, M.; Mauri, F.; Piscanec, S.; Jian, D.; Novoselov, K. S.; Roth, S.; Geim, A. K. Raman Spectrum of Graphene and Graphene Layers. *Phys. Rev. Lett.* **2006**, *97*, 187401.

(52) Gupta, S.; Saxena, A. Nanocarbon materials: probing the curvature and topology effects using phonon spectra. *J. Raman Spectrosc.* **2009**, *40*, 1127−1137.

(53) Ferrari, A. C. Raman spectroscopy of graphene and graphite: Disorder, electron-phonon coupling, doping and nonadiabatic effects. *Solid State Commun.* **2007**, *143*, 47−57.

(54) Ferrari, A. C.; Basko, D. M. Raman spectroscopy as a versatile tool for studying the properties of graphene. *Nat. Nanotechnol.* **2013**, *8*, 235−246.

(55) Ferrari, A. C.; Robertson, J. Interpretation of Raman spectra of disordered and amorphous carbon. *Phys. Rev. B: Condens. Matter Mater. Phys.* **2000**, *61*, 14095.

(56) Eftekhari, A.; Garcia, H. The necessity of structural irregularities of the chemical applications of graphene. *Mater. Today Chem.* **2017**, *8*, 1−16.

(57) Kim, K.; Zhu, P.; Li, N.; Ma, X.; Chen, Y. Characterization of oxygen containing functional groups on carbon materials with oxygen K-edge X-ray absorption near edge structure spectroscopy. *Carbon* **2011**, *49*, 1745−1751.

(58) López-Urías, F.; Muñoz-Sandoval, E.; Reyes-Reyes, M.; Romero, A. H.; Terrones, M.; Morán-López, J. L. Creation of Helical Vortices during Magnetization of Aligned Carbon Nanotubes Filled with Fe: Theory and Experiment. *Phys. Rev. Lett.* **2005**, *94*, 216102.

(59) Morelos-Gómez, A.; López-Urías, F.; Muñoz-Sandoval, E.; Dennis, C. L.; Shull, R. D.; Terrones, H.; Terrones, M. Controlling high coercivities of ferromagnetic nanowires encapsulated in carbon nanotubes. *J. Mater. Chem.* **2010**, *20*, 5906−5914.

(60) Arya, V. P.; Prasad, V.; Kumar, P. S. A. Magnetic Properties of Iron Particles Embedded in Multiwall Carbon Nanotubes. *J. Nanosci. Nanotechnol.* **2009**, *9*, 5406−5410.

(61) Dillon, F. C.; Bajpai, A.; Koós, A.; Downes, S.; Aslam, Z.; Grobert, N. Tuning the magnetic properties of iron-filled carbon nanotubes. *Carbon* **2012**, *50*, 3674−3681.